ARTICLE

Facile Syntheses of Silver Thioantimonates Exhibiting Second-harmonic Generation Responses and Large Birefringence†

Received 00th January 20xx,
Accepted 00th January 20xx

DOI: 10.1039/x0xx00000x

Gang Yang,[a,b,#] Xingxing Jiang,[c,#] Chao Wu,[b,#] Zheshuai Lin,[c] Zhipeng Huang,[b] Mark G. Humphrey[d] and Chi Zhang*[,a,b]

Two chalcogenide crystalline compounds, $[enH_2][Ag_4Sb_2S_6]$ (en = ethylenediamine) and $[enH][Ag_2SbS_3]$, have been successfully synthesized by mild ionothermal and solvothermal means. $[enH][Ag_2SbS_3]$ crystallizes in the noncentrosymmetric (NCS) and polar space group *Pc*, and its linear and nonlinear optical (NLO) properties have been investigated for the first time. Second harmonic generation (SHG) measurements revealed that $[enH][Ag_2SbS_3]$ affords powder SHG performance of 2.5 × KDP @1064 nm and 0.2 × $AgGaS_2$ @2100 nm. Additional particle size *vs* SHG efficiency measurements indicate that $[enH][Ag_2SbS_3]$ is type-I phase-matchable. The calculated birefringence Δn is 0.177 at 1064 nm, which is sufficiently large (the largest value among NCS thioantimonates) to achieve phase matching. $[enH_2][Ag_4Sb_2S_6]$ crystallizes in the centrosymmetric space group $P2_1/c$ and its structure features a double-layered variant honeycomb-like anionic network parallel to the *ac* plane separated by $[enH_2]^{2+}$ cations. The optical band gaps of $[enH_2][Ag_4Sb_2S_6]$ and $[enH][Ag_2SbS_3]$ are measured to be 2.37 and 2.53 eV, respectively. Theoretical studies using density functional theory have been implemented to further elucidate the relationship between the band structure and NLO properties in $[enH][Ag_2SbS_3]$.

Introduction

Crystalline chalcogenides have been extensively studied because of their fascinating topological structures and their practical applications in optical, photocatalytic, and electronic fields.[1-6] In order to achieve these specific functions, durative efforts on developing new chalcogenides with variable components and unique structures have never been interrupted.[7,8] Thioantimonates are of particular interest because of their diverse structures and their unprecedented performance in nonlinear optics, photoluminescence, magnetism, etc.[9-15] In the structures of thioantimonates, the trivalent Sb^{3+} cation is favored to feature a wide range of coordination numbers from 3 to 6, which would undergo self-condensation to construct new secondary building units (SBUs) that give rise to novel chalcogenides with remarkable topologies. Moreover, the Sb^{3+} cation with the stereochemically active lone-pair electrons is likely to induce the formation of noncentrosymmetric (NCS) structures, which may result in interesting physical nonlinear optical (NLO) properties.[16,17] Efforts have been made on the integration of transition metal (TM = Cr, Mn, Fe, Co, Ni, Zn, Cu, and Ag) atoms into thioantimonate compounds, which can not only enhance the structural diversity but also integrate the electronic, optical, and magnetic properties of TM atoms with the host inorganic framework.[18-26] However, the majority of thioantimonates are synthesized by hydro(solvo)thermal methods. In order to achieve practically applied thioantimonates with unique structures and enhanced properties, the innovation of synthetic approaches is highly desired.

Generally, crystalline chalcogenides can be prepared through several conventional methods, including flux synthesis methods,[27,28] hydro(solvo)thermal methods,[29-31] high-temperature solid-state reactions,[32,33] and room temperature solution method.[34] Among which, hydro(solvo)thermal synthesis represents a mild and soft synthetic technique with the merits of both kinetic and thermodynamic controllable during the reaction process.[35,36] Many crystalline ternary or quaternary chalcogenides with diverse structures and properties have been prepared under hydro(solvo)thermal condition.[37-39] Unlike molecular solvents, ionic liquids possess unique properties such as good ionic conductivity, low vapor pressure and high thermal stability, which have been demonstrated as a promising synthetic media in the exploration of novel crystalline zeolites, metal organic frameworks, and oxides in recent years.[40-43] The ionothermal synthesis approach that employs ionic liquids as the reaction solvents has also been applied in the preparation of new metal chalcogenides.[44] We recently reported two mid-IR NLO silver thioantimonates, which has demonstrated that synthetic factors including reaction temperature and pressure, reactant concentration and nature

[a] *China-Australia Joint Research Center for Functional Molecular Materials, School of Chemical and Material Engineering, Jiangnan University, Wuxi 214122, P. R. China.*
[b] *School of Chemical Science and Engineering, Tongji University, Shanghai 200092, P. R. China. Email： chizhang@tongji.edu.cn*
[c] *Key Lab of Functional Crystals and Laser Technology, Technical Institute of Physics and Chemistry, Chinese Academy of Sciences, Beijing 100190, China*
[d] *Research School of Chemistry, Australian National University, Canberra, ACT 2601, Australia*
[#] *G.Y., X.X.J. and C.W. contribute equally to this work.*
† Electronic Supplementary Information (ESI) available: CCDC 2041843-2041844. For ESI and crystallographic data in CIF or other electronic format See DOI: 10.1039/x0xx00000x

of the starting materials, redox potential, and reaction time have significantly influences on the formation of the silver thioantimonates under ionothermal condition.[45] However, the effects of the specific ionic liquids on the growth of functional crystalline chalcogenides is still unclear.

In this study, two silver thioantimonate crystals, $[enH_2][Ag_4Sb_2S_6]$ (en = ethylenediamine) (**1**) and $[enH][Ag_2SbS_3]$ (**2**), have been successfully synthesized by convenient ionothermal and solvothermal routes and fully characterized by various kinds of spectroscopic methods. The effect of ionic liquids on the crystalline structures and optical properties of chalcogenides have been explored. **2** crystallizes in NCS space group *Pc* and possesses moderate SHG efficiency both at 1064 and 2100 nm laser radiations. The calculated birefringence for **2** is 0.177 (the largest value among NCS thioantimonates) at 1064 nm, which is sufficiently large to achieve phase matching. Theoretical studies have also been carried out for the further understanding of the correlation between their NLO properties and band structures.

Experimental

Reagents

All reagents including S Powder (99%), Ag Powder (99%), Sb Powder (99.5%), and ethylenediamine (99%) were purchased commercially and used without further purification. The ionic liquid [HDMEA][CH_3COO] (DMEA = *N*,*N*-dimethylethanolamine) was prepared by a mixture of CH_3COOH (30 g, 0.5 mol) and DMEA (49 g, 0.55 mol) in a 200 mL flask at room temperature with stirring for ca. 2 hours.

Ionothermal synthesis of $[enH_2][Ag_4Sb_2S_6]$ 1

A stoichiometric mixture of Ag powder (0.108 g, 1.00 mmol), Sb powder (0.061 g, 0.50 mmol), S powder (0.192 g, 6.00 mmol), ethylenediamine (1.0 g, 16.5 mmol) and [HDMEA][CH_3COO] (1.00 g, 6.5 mmol) was sealed in an autoclave equipped with a Teflon liner (15 mL) and heated at 160 °C for 3 days, and then slowly cooled to room temperature at a rate of 4 °C/h. After the reaction, the products were filtered and washed several times with deionized water. Yellow flake-shaped crystals of **1** were isolated using a microscope with a yield of ~70% (based on Ag) (Fig. 1a). These crystals were stable for more than a month in a dark dry place.

Solvothermal synthesis of $[enH][Ag_2SbS_3]$ 2

The same procedure was employed to synthesize **1** except using ethylenediamine (1.00 g, 16.5 mmol) as the solvent. Dark yellow flake-shaped crystals of **2** with a yield of ~79% (based on Ag) were obtained (Fig. 1b).

Structural determination

The suitable single crystals of **1** and **2** for data collection were selected and cut in simethicone for gaining desired dimensions, which were then adhered to a glass fiber. Crystal structure determination of these compounds was performed on a Bruker

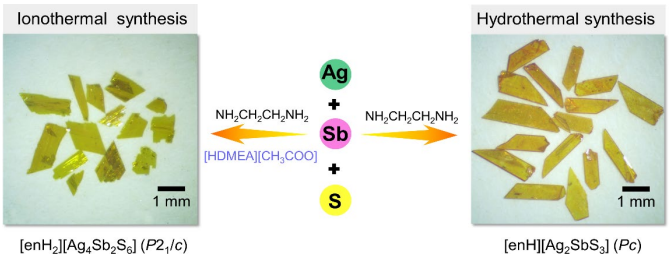

Fig. 1 Reaction routes, photographs, chemical formulae, and space group of the as-obtained silver thioantimonates **1** and **2**.

D8 VENTURE CMOS X-ray diffractometer equipped with graphite-monochromated Mo-Kα radiation (λ = 0.71073 Å) at room temperature with a ω-scan method. Data integration and cell refinement were performed by the INTEGRATE program with APEX II software, and multi-scan absorption correction were carried out using the SCALE program for area detector.[46] Semi-empirical from equivalents corrections were applied for all data sets using the APEX II program. The structures were solved by direct methods and refined on F^2 by full-matrix least-squares methods using the SHELXTL-*97* software package.[47] The crystal structure of **2** has been studied by P. Vaqueiro et al., however, because of the poor crystal quality and incomplete crystal data reported,[48] we re-collected the crystallographic data and re-determined the crystal structure. The structure was checked for missing symmetry elements using PLATON.[49] All of the non-hydrogen atoms were refined with anisotropic thermal displacement coefficients. N(1) and N(2) in **1** and N(2) in **2** were assigned as protonated $[NH_3]^+$ groups on the basis of the

Table 1 Crystallographic data and refinement details for **1** and **2**.[a]

	1	**2**
Empirical formula		
Formula weight	929.46	494.78
Temperature (K)	293(2) K	293(2) K
Crystal system	monoclinic	monoclinic
Space group	$P2_1/c$	Pc
a (Å)	6.4223(3)	6.1891(12)
b (Å)	19.5157(8)	11.953(2)
c (Å)	6.7998(3)	7.422(3)
α (°)	90	90
β (°)	117.5330(10)	119.46(2)
γ (°)	90	90
Volume (Å^3)	755.73(6)	478.1(2)
Z	2	2
Density (calculated) (g·cm^{-3})	4.085	3.437
Absorption coefficient (mm^{-1})	9.406	7.448
F(000)	844	456
Theta range for data collection (°)	3.54-27.50	3.41-27.50
Limiting indices	-8 ≤ h ≤ 8, -25 ≤ k ≤ 25, -8 ≤ l ≤ 8	-8 ≤ h ≤ 7, -15 ≤ k ≤ 15, -9 ≤ l ≤ 9
R_{int}	0.0404	0.0611
Reflections collected/unique	13582/1729	8335/2076
Goodness-of-fit on F^2	0.984	1.086
Final R indices [$F_o^2 > 2\sigma(F_o^2)$][a]	0.0377/0.0836	0.0392/0.0552
R indices (all data)[a]	0.0457/0.0876	0.0605/0.0591
Largest diff. peak and hole (e Å^{-3})	1.888 and -2.722	0.953 and -1.203

[a] $R_1 = \sum||F_o| - |F_c||/\sum|F_o|$; $wR_2 = [\sum w(Fo^2 - Fc^2)^2]/\sum w(Fo^2)^2]^{1/2}$

requirements of charge balance. Crystal data and structural refinement information are listed in Table 1. The positional coordinates together with isotropic equivalent thermal parameters of crystals **1** and **2** are given in Table S1†. Selected important bond distances (Å) and angles (deg) are summarized in Tables S2† and S3†.

Powder XRD

The powder XRD data of **1** and **2** were recorded on a Bruker-AXS D8 ADVANCE diffractometer equipped with Cu Kα (λ = 1.5418 Å) radiation at room temperature with the scanning range of 5–50° in 2ϑ and a scan step of 4°/min (Fig. S1†).

Energy-Dispersive X-ray spectroscopy

Microprobe elemental analyses were performed using energy-dispersive X-ray spectroscopy (EDS) with a field-emission scanning electron microscope (Hitachi S-4800, Japan). The EDS analyses on single crystals of **1** and **2** confirm the presence of N, Ag, Sb, and S, the amounts of each matching well with those determined from the single-crystal X-ray structure studies (Fig. S2†).

Infrared spectroscopy

The Fourier transform infrared (FTIR) spectra of **1** and **2** were collected on a Nicolet iS10 Fourier transform IR spectrometer in the range of 500 to 4000 cm^{-1} at room temperature. The samples were mixed thoroughly with dried KBr and were then pressed into discs for measurements.

UV-Vis-NIR diffuse reflectance spectra

The UV-Vis-NIR diffuse reflectance spectra for **1** and **2** were recorded using a Cary 5000 UV-Vis-NIR spectrophotometer in the range of 200–2500 nm at room temperature. A $BaSO_4$ plate was used as a standard (100% reflectance) for the baseline correction. The absorption spectra were calculated from the diffuse reflectance spectra based on the Kubelka–Munk function: $\alpha/S = (1 - R)^2/2R$,[50] in which R is the reflectance coefficient, α is the absorption coefficient and S is the scattering coefficient.

Second-Order NLO measurements

SHG measurements on a powder crystalline samples of **1** and **2** were carried out with the modified Kurtz and Perry powder method,[51] employing 1064 nm and 2100 nm lasers as the radiation lights. The samples were ground and sieved by a series of mesh sizes at the range of 26–50, 50–74, 74–105, 105–150 and 150–200 μm, respectively. Crystalline KH_2PO_4 (KDP) and $AgGaS_2$ were also ground and sieved into the same particle size ranges and used as the reference for the SHG signals. These samples were pressed into disks with diameters of 6 mm that was put between glass microscope slides and secured with tape in a 1 mm thick aluminum holder.

Computational method

The first-principles simulations were performed using CASTEP,[52] a plane-wave pseudopotential total energy package based on DFT.[53,54] The functional developed by Perdew, Burke, and Ernzerhof[55] in the generalized gradient approximation[56] form was adopted to describe the exchange–correlation energy. The optimized norm-conserving pseudopotentials[57] in the Kleinman–Bylander form were adopted to model the effective interaction between the valence electrons and atom cores, which allows the choice of a relatively small plane-wave basis set without compromising the computational accuracy. A kinetic energy cutoff of 800 eV and Monkhorst–Pack[58] k-point mesh spanning less than 0.03 $Å^{-1}$ in the Brillouin zone were chosen. Detailed theoretical calculations are shown in the ESI†.

Results and discussion

Synthesis of 1 and 2

Preparation of functional crystalline chalcogenides under mild synthetic methods is urgently pursued because the conventional high-temperature solid-state synthesis suffers from the disadvantages such as high energy consumption and lengthy reactions. In this work, two kinds of mild synthetic methods (ionothermal and solvothermal methods) under the similar synthetic condition were adopted to prepare silver thioantimonates. Specifically, with the same starting materials of Ag powder (1 mmol), Sb powder (0.5 mmol), S powder (6 mmol), **1** and **2** can be isolated as single phases via ionothermal and solvethermal reactions, respectively. Indeed, the only

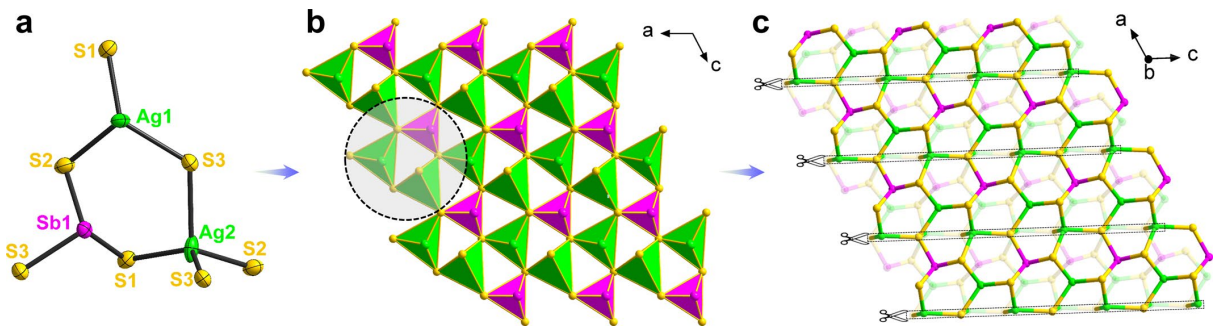

Fig. 2 (a) $[Ag_2SbS_7]^{9-}$ cluster unit. (b) Polyhedral view of a $[Ag_2SbS_3]^-$ layer along the *b*-axis in **1**. (c) View of a $[Ag_4Sb_2S_6]^{2-}$ double layer formed from linkage of two variant honeycomb-like sheets via Ag–S bonds along the *b*-axis. Each sheet is comprised of 6-membered Ag-Sb-S rings.

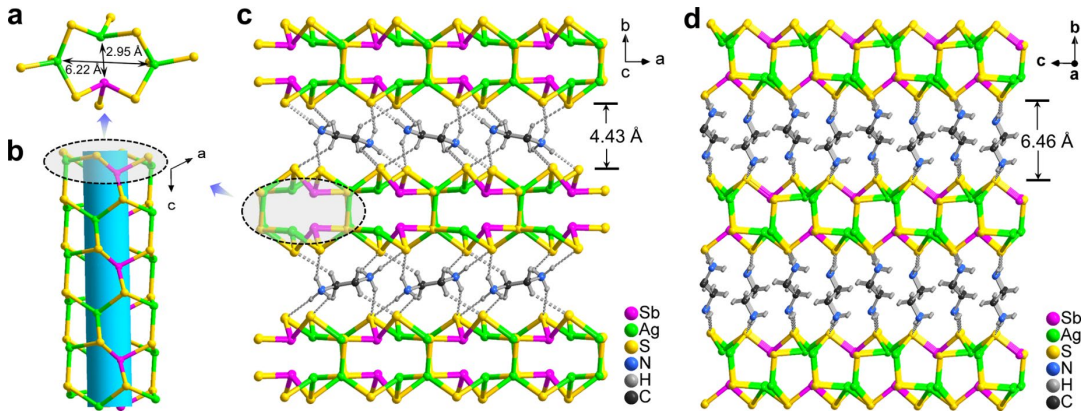

Fig. 3 (a) The 8-membered crownlike rings. (b) View of the 8-membered ring channel in **1** along the *c*-axis. (c) View of the packing structure of **1** with the $[enH_2]^{2+}$ cations located in the interlayer space along the *c*-axis. (d) View of the packing structure of **2** with the $[enH]^{+}$ cations located in the interlayer space along the *c*-axis.

difference between the synthetic procedures of **1** and **2** is the additional use of ionic liquid [HDMEA][CH_3COO] in **1**. To better understand the influence of reaction conditions (including ionic liquid, the amount of the starting materials, reaction temperatures) on the target compounds, systematic synthesis experiments have been performed on chalcogenide Ag-Sb-S system. Some hints could be summarized as follows: (i) Different antimony source with equal amount could achieve the same products under the same conditions. (ii) Reaction temperature may affect the formation of final production. Specifically, **2** could always be obtained in the temperature range of 140~190 °C, while it is hard to obtain the pure **1** when the reaction temperature adopted higher than 180 °C. (iii) Ionic liquids could affect the formation of crystalline chalcogenides. Unlike **2**, the synthesis of **1** requires ionic liquid [HDMEA][CH_3COO], suggesting that ionic liquid can induce the formation of different structure building units and thereby lead to distinct crystal structures eventually. These results indicate that the ionic liquid [HDMEA][CH_3COO] and suitable reaction temperature play the key roles in constructing silver thioantimonates with various kinds of structural compositions and molecular configurations.

Structure of 1

Single-crystal X-ray diffraction analysis reveals that **1** belongs to centrosymmetric monoclinic space group $P2_1/c$ (No. 14) and features an anionic double-layered network parallel to the *ac* plane separated by protonated $[enH_2]^{2+}$ cations (Fig. 2c). The asymmetric unit of **1** contains one crystallographically independent Sb^{3+} cation, two Ag^{+} cations, three S^{2-} anions, and half of $[enH_2]^{2+}$ cation. Each Sb atom is coordinated by three S atoms to form [SbS_3] triangular pyramid with Sb−S bond distances in the range 2.4059(18)−2.4444(18) Å. Ag(1) shows a trigonal pyramid geometry while Ag(2) presents a tetrahedrally coordination geometry, among which the Ag−S bond lengths range from 2.5427(18) to 2.653(2) Å for Ag(1) and from 2.5628(19) to 2.770(2) Å in Ag(2), respectively. The Sb−S and Ag−S bond lengths are comparable to those in the reported silver thioantimonates.[23-26]

In the silver thioantimonate crystal, the primary building units (PBUs) − the six-membered [Ag_2SbS_7] units are composed of one [SbS_3], one [AgS_3], and one [AgS_4] units linked via bridging S atoms (Fig. 2a). Further connectivity of the [Ag_2SbS_7] PBUs through their vertices yields a variant 2D honeycomb-like sheet in the *ac* plane (Fig. 2b). The anionic $[Ag_4Sb_2S_6]_\infty$ double-layer of **1** is formed by the combination of two variant honeycomb-like $[Ag_2SbS_3]_\infty$ layers that are joined by Ag(2)−S(3) bonds (Fig. 2c). As a result, an interesting rectangular 8-membered ring (8-MR) channel is observed in **1** running along the *c*-axis (Fig. 3b). The 8-membered crownlike ring exhibits a rough square cross-section of 2.95 × 6.22 $Å^2$ (Fig. 3a).

The [enH_2] cations as charge-balancing agents and structural directing agents are located in the interlayered spaces, and form extensive N−H···S and C−H···S hydrogen bonds with S atoms of the anionic framework (Fig. 3c). The N−H···S hydrogen bond distances and angles fall in the range of 3.1129−3.5897 Å and 114.0−170.0°, respectively (Table S4†). The C−H···S hydrogen bond distance and angle are 3.5478 Å and 136.0°, respectively. After the removal of all organic cations in the interlayered spaces, the effective solvent accessible volume occupies 12% of the total cell volume calculated by the PLATON program.[49]

Structure of 2

2 crystallizes in the acentric space group *Pc*. The asymmetric unit of **2** contains one Sb^{3+} cation, two Ag^{+} cations, three S^{2-} anions, and a $[enH]^{+}$ cation. Each Sb atom is bonded to three S atoms to form the [SbS_3] triangular pyramid (Fig. 4h). There are two different kinds of coordination geometries for the two d^{10} transition-metal Ag^{+} cations. The first type of Ag^{+} adopts the [SbS_3] trigonal-pyramidal coordination geometry (Fig. 4g), while the second type of Ag cations possess [AgS_3] triangular coordination geometry (Fig. 4f). These [SbS_3] triangular pyramids, [AgS_3] triangular pyramids, and [AgS_3] triangles are then linked by a sulfur vertex forming the $[Ag_2SbS_3]_\infty$ single-layer with alternately interlinking 6-MRs and 10-MRs (Fig. 4b). The $[Ag_2SbS_3]_\infty$ single-layers are connected by [AgS_3] units to

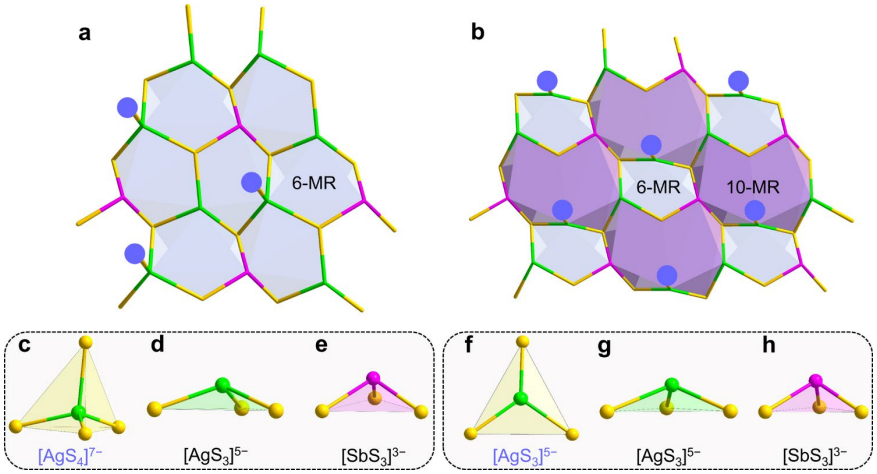

Fig. 4 (a) View of the $_{\infty}[Ag_2SbS_6]^{7-}$ anionic layer with 6-MRs in **1**. (b) View of the $_{\infty}[Ag_2SbS_6]^{7-}$ anionic layer with 6-MRs and 10-MRs in **2**. The light blue balls present the sites that connect to adjacent $_{\infty}[Ag_2SbS_6]^{7-}$ anionic layers. (c-e) Coordination environments of the Ag and Sb atoms in **1**. (f-g) Coordination environments of the Ag and Sb atoms in **2**.

form a lamellar structure in the *ac* plane with the [enH] cations locating in the interlayered spaces (Fig. 3d).

Synthetic methods influencing macroscopic centricities and the framework structures

Crystalline compounds **1** and **2** have the similar composition, including protonated ethylenediamine molecules and $[Ag_2SbS_3]$ units, but they exhibit distinct centricities (**1**: $P2_1/c$; **2**: Pc). The latter can be attributed to the flexible coordination environments of Ag atoms. Specifically, the Ag atoms in **1** adopt two coordination geometries in the $[Ag(1)S_3]$ trigonal pyramid (Fig. 4d) and $[Ag(2)S_4]$ tetrahedron (Fig. 4c), while the Ag atoms in **2** are connected with three sulfur atoms to generate $[Ag(1)S_3]$ triangle (Fig. 4f) and $[Ag(2)S_3]$ trigonal pyramid (Fig. 4g). All the Sb atoms in both two compounds adopt $[SbS_3]$ trigonal-pyramidal coordination geometries (Figs. 4e and 4h). Further connectivity of $[AgS_4]$, $[AgS_3]$, and $[SbS_3]$ units in **1** through their vertices yields a variant honeycomb-like network with 6-MRs (Fig. 4a). In contrast, vertex-linking of $[SbS_3]$ and two types of $[AgS_3]$ units in **2** produces a 2D $[Ag_2SbS_3]_{\infty}$ layer with 6-MRs and 10-MRs (Fig. 4b). The anionic double-layers of **1** and **2** are formed by the combination of two single $[Ag_2SbS_3]_{\infty}$ layers that are joined by $[AgS_4]$ and $[AgS_3]$ units, respectively. Charge compensation requires that the ethylenediamine molecules are diprotonated in **1** and monoprotonated in **2**. The protonated ethylenediamine cations as charge-balancing agents and structural directing agents are located in the interlayered spaces. The distance between the adjacent double-layers of **1** (4.43 Å) is clearly smaller than that of the double-layers of **2** (6.46 Å) (Fig. 3a), indicating that the extensive N−H···S hydrogen bonds formed between protonated ethylenediamine species and metal sulfur layers make great contributions to the stabilization of **1**.

From the synthesis of **1** and **2**, it demonstrates that ionic liquid [HDMEA][CH_3COO] have a significant influence on the crystal growth of silver thioantimonates, and thereby interesting structural transformation occurs in the silver thioantimonates from centrosymmetric (CS) structure in **1** by ionic liquid to NCS architecture of **2** without ionic liquid. The coordination environments of Ag atoms are also influenced by adding ionic liquid [HDMEA][CH_3COO] owing to the strong interactions between [CH_3COO] groups and chalcogenide species. Ionic liquid [HDMEA][CH_3COO] also change the connection modes of *in situ* generated structure building units such as PBUs ($[Ag_2SbS_7]$ in **1** and $[Ag_2SbS_6]$ of **2**) and hydrogen bonds.

Powder X-ray diffraction

The powder X-ray diffraction (PXRD) patterns of **1** and **2** were recorded (Fig. S1†). The measurement results show that the PXRD pattern of the as-synthesized product matches very well with the simulated patterns generated using the CIF of each refined structure, indicating the phase purity of the products. The differences in intensity may be due to the preferred orientation of the powder samples.

UV-Vis-NIR diffuse reflectance spectra

The UV-Vis-NIR diffuse reflectance data (Fig. 5) show that the optical band gaps for **1** and **2** are 2.37 and 2.53 eV, respectively, which are consistent with their yellow colors. The distinct band

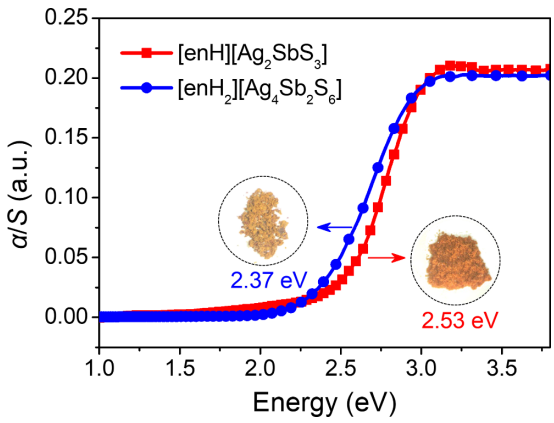

Fig. 5 Optical band gaps for **1** and **2**.

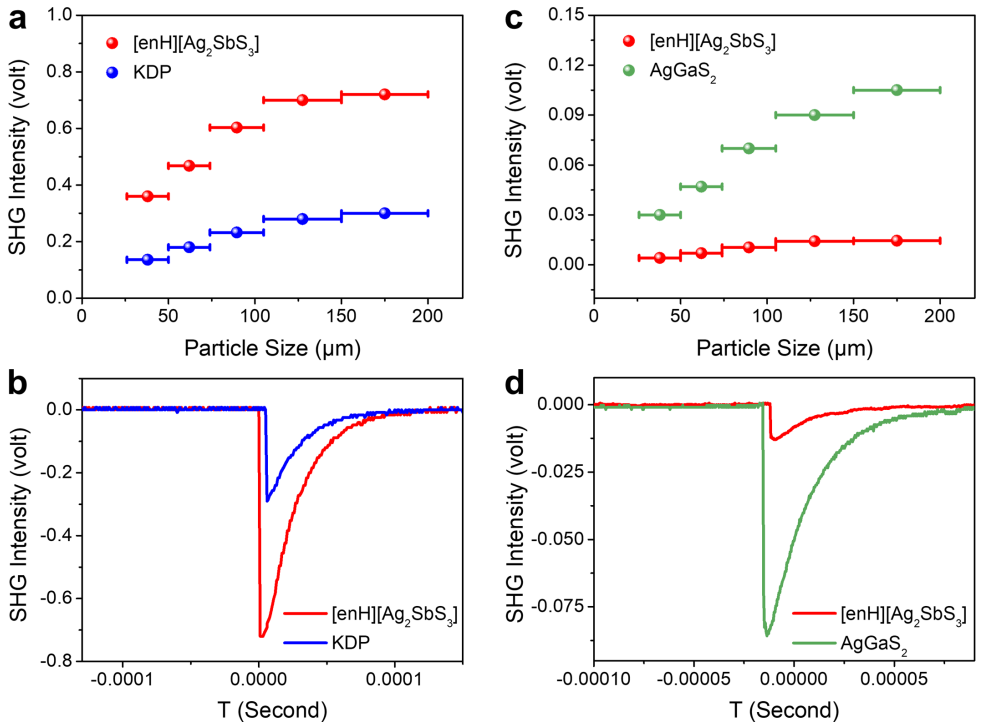

Fig. 6 Phase-matching curves of **2** with 1064 nm (a) and 2100 nm (c) laser radiation. Oscilloscope traces of the SHG signals for powders of **2** (105−150 μm) with 1064 nm (b) and 2100 nm (d) laser radiation. KDP and $AgGaS_2$ were used as references for the SHG measurements at 1064 and 2100 nm, respectively.

gaps of **1** and **2** might be due to the differences in their structures and compositions. These values are close to those of the $[Co(en)_3]_3(en)In_6Sb_6S_{21}\cdot H_2O$ (2.46 eV),[59] $[(CH_3CH_2CH_2)_2NH_2]_5In_5Sb_6S_{19}\cdot 1.45H_2O$ (2.62 eV),[60] and $[Ni(en)_3][InSbS_4]$ (2.84 eV).[61]

IR spectra

The IR spectra of the two crystalline materials **1** and **2** are displayed in Fig. S3†. The absorption bands observed between 3650 and 3097 cm^{-1} are assigned to the N−H stretching vibrations whereas other bands observed between 1697 and 1382 cm^{-1} are ascribed to the bond bending of N−H. In addition, the strong peak at about 982 cm^{-1} can be assigned to the stretching vibrations of C−N bonds. The bands at 1145 cm^{-1} originate from NH_2 rocking in **2**. The absorptions located at 1048, 1450, 1570, 3250, and 3444 cm^{-1} are typical for R-NH_3^+ groups, confirming the presence of protonated ethylenediamine cations.[62]

SHG properties

The crystal structures of **1** and **2** are significantly influenced by the different synthetic methods. The NCS and polar structure of **2**, composed of monoprotonated ethylenediamine, $[SbS_3]$ triangular pyramids, $[AgS_3]$ triangular pyramids, and unique $[AgS_3]$ triangles, encouraged us to examine its SHG properties. After sieving the crystalline samples into five different particle size ranges, SHG measurements reveal that its SHG intensities increase with increasing particle size before they reach maxima that are independent of particle size under 1064 nm and 2100 nm laser radiation (Figs. 6a and 6c), indicating that **2** is a type-I phase-matchable material. The SHG efficiencies of **2** are 2.5 × KDP at 1064 nm (Fig. 6b) and 0.20 × $AgGaS_2$ at 2100 nm (Fig. 6d), respectively. The SHG efficiency is comparable to that of $[TMDPH_2][As_4S_6]$ (2.0 × KDP with type-I phase matchability).[63] It should be noted that the stereochemically active lone-pair cation Sb^{3+} make less contribution to the NLO response because the $[SbS_3]$ units in the 2D $[Ag_2SbS_3]_\infty$ layers are almost aligned in antiparallel fashion. In addition, the arrangements of $[AgS_3]$ and $[SbS_3]$ units in the 2D layers are also not favorably aligned. As a consequence, a modest SHG response for **2** is observed.

Structure-optical property relationships

To obtain more insight into the microscopic mechanism of the optical performance of **2**, first-principles calculations based on pseudopotential DFT were performed.[53,54] The calculated band structure reveals that **2** is an indirect transition band material. The minimum of the lowest unoccupied molecular orbital (LUMO) and the maximum of the highest occupied molecular orbital (HOMO) are located at Y line and near E line, respectively (Fig. 7a). The band structure calculation suggests band gap of 2.14 eV for **2**, which is slightly smaller than its experimental band gap (2.53 eV). The total and partial DOS of **2** are displayed in Fig. 7b. The valence band (VB) and conduction band (CB) near the Fermi energy (−10 to 10 eV) have been investigated because these areas comprise the majority of the bonding interactions. In the VB region (−10 eV to Fermi level), the S-3p and Ag-4d states make the main contributions, mixed with small amounts of the Sb-5p, N-2s, C-2s, and H-1s states. The CB region (Fermi level to 10 eV) is mainly originated from Ag-5s, S-3p, Sb-5s and 5p states, as well as small amounts of C-2p, N-2p and H-1s

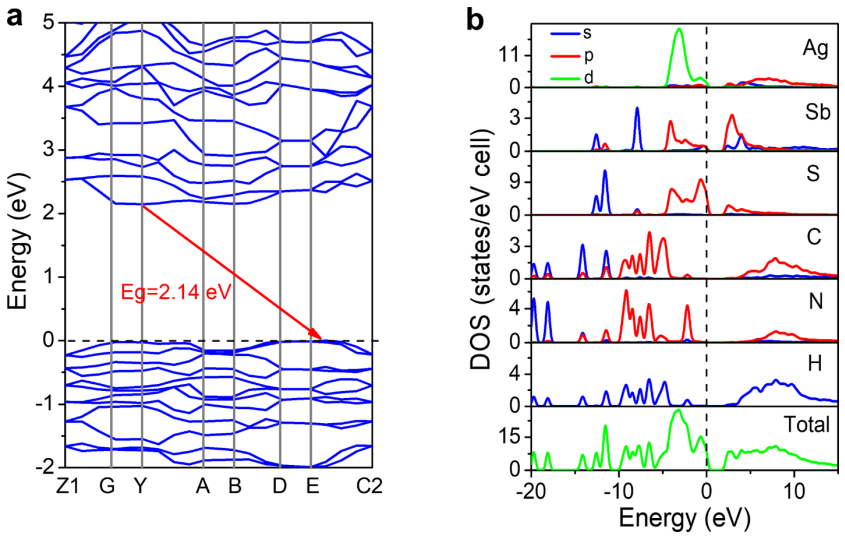

Fig. 7 (a) Calculated band structure of **2**, the Fermi level is set at 0 eV. (b) Partial and total density of states of **2**.

states. Therefore, the band gap of **2** is mainly ascertained by Ag, Sb, S atoms, and protonated ethylenediamine molecules.

The calculated refractive index dispersion curve of **2** is shown in Fig. 8a. The sequence of refractive indices is in the order of $n_x > n_z > n_y$, and the birefringence is calculated to be 0.177 at 1064 nm, which is favorable for the phase matching in SHG. Such a birefringence of **2** is comparable to those of $A_2Ag_3Sb_3S7$ (A = Rb, Cs),[45] and significantly larger than those of NCS phase-matchable thioantimonates (e.g., $Ba_3(BS_3)(SbS_3)$ (0.05 static),[64] KAg_2SbS_4 (0.053 @ 1064 nm)[65]). Under the restriction of Kleinman's symmetry[66] and point group *m*, there are six independent SHG tensor components (d_{11}, d_{12}, d_{13}, d_{15}, d_{24}, and d_{33}). The calculated six frequency-dependent NLO components[67] of the **2** were plotted in Table S6†. The values of d_{11}, d_{12}, d_{13}, d_{15}, d_{24}, and d_{33} at a wavelength of 1064 nm are -25.21, -4.64, 5.27, 12.17, 1.68 and -9.58 pm/V, respectively, which is much higher than the measured value. It is reasonable because the SHG coefficients are calculated by the periodic crystal whereas the experimentally measured SHG signal is based on the powder sample. To further investigate the principal source of the SHG response, a SHG-weighted electronic density analysis was performed to display the electronic orbitals which affect the SHG response. The SHG-weighted electronic clouds are mainly located on the $[SbS_3]$ and $[AgS_3]$ groups but are almost absent from the [Hen] cations. For the occupied states, the orbitals in the $[SbS_3]$ groups make dominant contributions to the SHG response (Fig. 8b), while for the unoccupied states the orbitals in $[AgS_3]$ groups are the major sources of the SHG response (Fig. 8c). Moreover, a real-space atom-cutting technique[68] was adopted to analyze the respective contribution of groups to the nonlinear optical properties. The result is shown in the Table S6†, which supports the conclusion from SHG-weighted electron density analysis that the SHG response of **2** is attributable to the synergistic effect of NLO-active $[SbS_3]$ and $[AgS_3]$ units.

Conclusions

In summary, 2D silver thioantimonate compounds containing protonated ethylenediamines, **1** and **2**, were successfully synthesized by a convenient ionothermal and solvothermal means. The different solvent systems (en/[HDMEA][CH_3COO], and en) employed in the syntheses may result in diversity in the framework structures. **1** crystallizes in the centrosymmetric

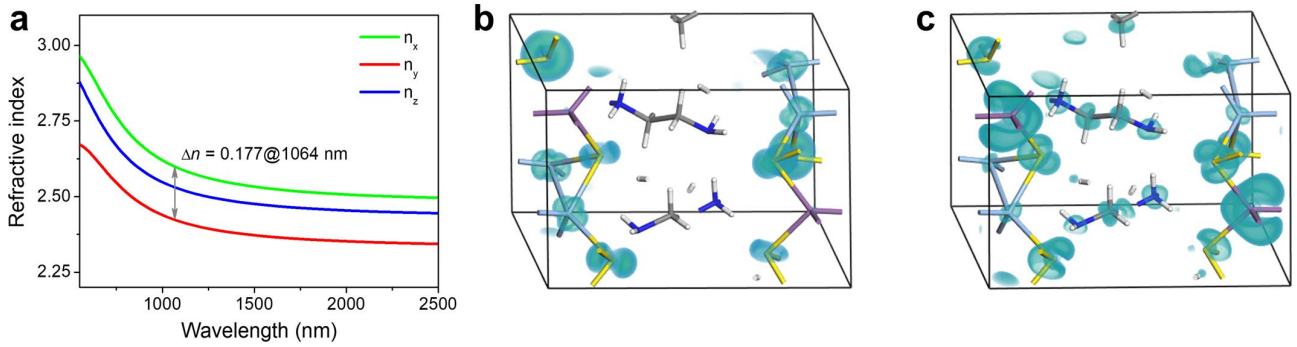

Fig. 8 (a) Calculated refractive index dispersion curve of **2**. SHG-weighted density for (b) occupied and (c) unoccupied states in the virtual electron process.

space group $P2_1/c$ and features a double-layered variant honeycomb-like anionic network separated by [enH_2] cations. In contrast, **2** crystallizes in the polar space group *Pc* and its linear and NLO properties have been systematic investigated. The optical band gaps of **1** and **2** are measured to be 2.37 and 2.53 eV, respectively, which are consistent with their colors and the calculated results. The polycrystalline samples exhibit a moderate intensity phase-matchable SHG responses of 2.5 times greater than KDP at a laser radiation of 1064 nm and 0.2 × $AgGaS_2$ at a laser radiation of 2100 nm. The first-principles calculations were also carried out to the further elucidate that SHG response of **2** can be attributed to the synergistic effect of NLO-active [SbS_3] and [AgS_3] units. The calculated birefringence indexes Δ*n* are 0.177 at 1064 nm for achieving phase matching, which is the largest value among NCS thioantimonates. This study indicates that mild ionothermal/solvothermal methods are the applicable strategies to prepare promising functional chalcogenides with various kinds of structural compositions and molecular configurations.

Conflicts of interest

There are no conflicts to declare.

Acknowledgements

This research was financially supported by the National Natural Science Foundation of China (No. 51432006), the Ministry of Education of China for the Changjiang Innovation Research Team (No. IRT14R23), the Ministry of Education and the State Administration of Foreign Experts Affairs for the 111 Project (No. B13025), and the Innovation Program of Shanghai Municipal Education Commission. M.G.H. thanks the Australian Research Council for support (DP170100411).

Notes and references

1 N. F. Zheng, X. G. Bu, B. Wang and P. Y. Feng, *Science* 2002, **298**, 2366-2369.
2 T. K. Bera, J. I. Jang, J. B. Ketterson and M. G. Kanatzidis, *J. Am. Chem. Soc.*, 2009, **131**, 75-77.
3 J. Zhou, *Coord. Chem. Rev.* 2016, **315**, 112-134.
4 L. N. Nie and Q. C. Zhang, *Inorg. Chem. Front.*, 2017, **4**, 1953-1962.
5 S. P. Guo, Y. Chi and H. G. Xue, *Angew. Chem. Int. Ed.*, 2018, **57**, 11540-11543.
6 R. H. Duan, P. F. Liu, H. Lin, Y. J. Zheng, J. S. Yu, X. T. Wu, S. X. Huang-Fu and L. Chen, *J. Mater. Chem. C*, 2017, **5**, 7067-7074.
7 W. W. Lin, C. C. Stoumpos, O. Y. Kontsevoi, Z. F. Liu, Y. H. He, S. Das, Y. D. Xu, K. M. McCall, B. W. Wessels and M. G. Kanatzidis, *J Am Chem Soc.*, 2018, **140**, 1894-1899.
8 W. H. Xing, N. Z. Wang, Y. W. Guo, Z. Li, J. Tang, K. J. Kang, W. L. Yin, Z. S. Lin, J. Y. Yao and B. Kang, *Dalton Trans.*, 2019, **48**, 17620-17625.
9 H. J. Zhao, Y. F. Zhang and L. Chen, *J. Am. Chem. Soc.*, 2012, **134**, 1993-1995.
10 C. Wu, X. X.Jiang, L. Lin, Z. S. Lin, Z. P. Huang, M. G. Humphrey, and C. Zhang, *Chem. Mater.* 2020, **32**, 6906-6915.
11 A. Abudurusuli, K. Wu, A. Tudi, Z. H. Yang and S. L. Pan, *Chem. Commun.*, 2019, **55**, 5143-5146.
12 J. Zhou, J. Dai, G. Q. Bian, C. Y. Li, *Coord. Chem. Rev.*, 2009, **253**, 1221-1237.
13 Y. J. Lin, B. W. Liu, R. Ye, X. M. Jiang, L. Q. Yang, H. Y. Zeng and G. C. Guo, *J. Mater. Chem. C*, 2019, **7**, 4459-4465.
14 H. Lee and K. M. Ok, *Bull. Korean Chem. Soc.* 2020, **41**, 139-142.
15 J. Y. Chung, H. Jo, S. Yeon, H. R. Byun, T. S. You, J. I. Jang and K. M. Ok, *Chem. Mater.* 2020, **32**, 7318-7326
16 M. C. Chen, L. M. Wu, H. Lin, L. J. Zhou and L. Chen, *J. Am. Chem. Soc.*, 2012, **134**, 6058-6060.
17 J. L. Mertz, N. Ding and M. G. Kanatzidis, *Inorg. Chem.*, 2009, **48**, 10898-10900.
18 M. L. Feng, D. Sarma, Y. J. Gao, X. H. Qi, W. A. Li, X. Y. Huang and M. G. Kanatzidis, *J. Am. Chem. Soc.*, 2018, **140**, 11133-11140.
19 K. Wu, B. B. Zhang, Z. H. Yang and S. L. Pan, *Chem. Commun.*, 2018, **54**, 8269-8272.
20 A. V. Powell, R. Paniagua, P. Vaqueiro, A. M. Chippindale, *Chem. Mater.*, 2002, **14**, 1220-1224.
21 C. Hu, B. B. Zhang, B. H. Lei, S. L. Pan and Z. H. Yang, *ACS Appl. Mater. Interfaces*, 2018, **10**, 26413-26421.
22 Y. Liu, X. D. Song, R. C. Zhang, F. Y. Zhou, J. W. Zhang, X. M. Jiang, M. Ji and Y. L. An *Inorg. Chem.*, 2019, **58**, 15101-15109.
23 C. Y. Yue, X. W. Lei, Y. X. Ma, N. Sheng, Y. D. Yang, G. D. Liu and X. R. Zhai, *Cryst. Growth Des.*, 2014, **14**, 101-109.
24 B. Zhang, W. A. Li, Y. Y. Liao, C. Zhang, M. L. Feng and X. Y. Huang, *Chem. Asian J.*, 2018, **13**, 672-678.
25 C. Y. Yue, X. W. Lei, R. Q. Liu, H. P. Zhang, X. R. Zhai, W. P. Li, M. Zhou, Z. F. Zhao, Y. X. Ma and Y. D. Yang, *Cryst. Growth Des.*, 2014, **14**, 2411-2421.
26 Q. T. Xu, Z. D. Sun, Y. Chi, H. G. Xue and S. P. Guo, *J. Mater. Chem. C*, 2019, **7**, 11752-11756.
27 X. Zhang, N. Yi, R. Hoffmann, C. Zheng, J. H. Lin and F. Q. Huang, *Inorg. Chem.*, 2016, **55**, 9742-9747.
28 M. G. Kanatzidis and A. C.Sutorik, *Prog. Inorg. Chem.*, 2007, **43**, 151-265.
29 R. C. Zhang, H. G. Yao, S. H. Ji, M. C. Liu, M. Ji and Y. L. An, *Chem. Commun.*, 2010, **46**, 4550-4552.
30 N. Pienack, A. Puls, C. Naether and W. Bensch, *Inorg. Chem.*, 2008, **47**, 9606-9611.
31 C. Wu, L. H. Li, L. Lin, Z. P. Huang, M. G. Humphrey and C. Zhang, *Dalton Trans.* 2020, **49**, 3253-3259.
32 R. Ye, X. Cheng, B. W. Liu, X. M. Jiang, L. Q. Yang, S. Q. Deng and G. C. Guo, *J. Mater. Chem. C*, 2020, **8**, 1244-1247.
33 X. L. Chen, Q. Jing and K. M. Ok, *Angew. Chem. Int. Ed.* 2020, **59**, 20323-20327.
34 J. F. Zhang, D. Jia, M. G. Humphrey, S. Meng, M. J. Zaworotko, M. P. Cifuentes and C. Zhang, *Chem. Commun.*, 2016, **52**, 3797-3800.
35 C. Wu, L. Lin, X. X. Jiang, Z. S. Lin, Z. P. Huang, M. G. Humphrey, P. S. Halasyamani and C. Zhang, *Chem. Mater.*, 2019, **31**, 10100-10108.
36 C. Wu, L. H. Li, L. Lin, Z. P. Huang, M. G. Humphrey and C. Zhang, *Chem. Mater.*, 2020, **32**, 3043-3053.
37 C. Zhang, K. N. Wang, M. Ji and Y. L. An, *Inorg. Chem.*, 2013, **52**, 12367-12371.
38 B. Zhang, J. Li, C. F. Du, M. L. Feng and X. Y. Huang, *Inorg. Chem.*, 2016 **55**, 10855-10858.
39 W. W. Xiong, J. W. Miao, P. Z. Li, Y. L. Zhao, B. Liu and Q. C. Zhang, *J. Solid State Chem.*, 2014, **218**, 146-150.
40 E. R. Cooper, C. D. Andrews, P. S. Wheatley, P. B. Webb, P. Wormald and R. E. Morris, *Nature*, 2004, **430**, 1012-1016.
41 K. Jin, X. Y. Huang, L. Pang, J. Li, A. Appel and S. Wherland, *Chem. Commun.*, 2002, 2872-2873.
42 X. X. Li, L. J. Zhang, C. Y. Cui, R. H. Wang and G. Y. Yang, *Inorg. Chem.*, 2018, **57**, 10323-10330.
43 T. G. Parker, A. L. Chown, A. Beehler, D. Pubbi, J. N. Cross and T. E. Albrecht-Schmitt, *Inorg. Chem.*, 2015, **54**, 570-575.

44 S. Santner, J. Heine and S. Dehnen, *Angew. Chem. Int. Ed.*, 2016, **55**, 876-893.
45 G. Yang, L. H. Li, C. Wu, M. G. Humphrey and C. Zhang, *Inorg. Chem.*, 2019, **58**, 12582-12589.
46 Bruker APEX2; Bruker AXS Inc.: Madison, WI, 2005.
47 G. M. Sheldrick, SHELXTL, crystallographic software package, version 5.1; Bruker-AXS: Madison, WI, 1997.
48 P. Vaqueiro, A. M. Chippindale, A. R. Cowley and A. V. Powell, *Inorg. Chem.*, 2003, **42**, 7846-7851
49 A. L. Spek, PLATON, a multipurpose crystallographic tool; Utrecht University: Utrecht, The Netherlands, 2001.
50 W. M. Wendlandt and H. G. Hecht, Reflectance Spectroscopy; Wiley Interscience: New York, 1966.
51 S. K. Kurtz and T. T. Perry, *J. Appl. Phys.*, 1968, **39**, 3798-3813.
52 S. J. Clark, I. Segall, C. J. Pickard, P. J. Hasnip, M. I. J. Probert, K. Refson and M. C. Payne, *Z. Kristallogr.*, 2005, **220**, 567-570.
53 W. Kohn and L. J. Sham, *Phys. Rev.*, 1965, **140**, A1133-A1138.
54 M. C. Payne, M. P. Teter, D. C. Allan, T. A. Arias and J. D. Joannopoulos, *Rev. Mod. Phys.*, 1992, **64**, 1045-1097.
55 J. P. Perdew, K. Burke and M. Ernzerhof, *Phys. Rev. Lett.*, 1996, **77**, 3865-3868.
56 J. P. Perdew and Y. Wang, *Phys. Rev. B: Condens. Matter Mater. Phys.*, 1992, **46**, 12947-12954.
57 D. R. Hamann, M. Schlüter and C. Chiang, *Phys. Rev. Lett.*, 1979, **43**, 1494-1497.
58 H. J. Monkhorst and J. D. Pack, *Phys. Rev. B: Solid State*, 1976, **13**, 5188-5192.
59 P. Vaqueiro, A. M. Chippindale and A. V. Powell, *Inorg. Chem.*, 2004, **43**, 7963-7965.
60 N. Ding and M. G. Kanatzidis, *Chem. Mater.*, 2007, **19**, 3867-3869.
61 M. L. Feng, P. X. Li, K. Z. Du and X. Y. Huang, *Eur. J. Inorg. Chem.*, 2011, 3881-3885.
62 V. Spetzler, C. Nather and W. Bensch, *J. Solid State Chem.*, 2016, **179**, 3541-3549.
63 D. D. Yang, Y. Song, B. Zhang, N. N. Shen, G. L. Xu, W. W. Xiong and X. Y. Huang, *Cryst. Growth Des.*, 2018, **18**, 3255-3262.
64 Y. Y. Li, B. X. Li, G. Zhang, L. J. Zhou, H. Lin, J. N. Shen, C. Y. Zhang, L. Chen, L. M. Wu, *Inorg. Chem.*, 2015, **54**, 4761-4767.
65 J. B. Huang, M. Mamat, S. L. Pan, Z. H. Yang, *J. Solid State Chem.*, 2016, **239**, 30-35.
66 D. A. Kleinman, *Phys. Rev.*, 1962, **126**, 1977-1979.
67 Z. S. Lin, J. Lin, Z. Z. Wang, Y. C. Wu, N. Ye, C. T. Chen and R. K. Li, *J. Phys. Condens. Matter*, 2001, **13**, 369-384.
68 R. He, Z. S. Lin, M. H. Lee, C. T. Chen, *J. Appl. Phys.*, 2011, **109**, 103510.